Optics Letters

Enhancement of silicon vacancy fluorescence intensity in silicon carbide using a dielectric cavity

Qi-Cheng Hu,[1,†] Ji Xu,[2,†] Qin-Yue Luo,[1] Hai-Bo Hu,[2] Pei-Jie Guo,[1] Cheng-Ying Liu,[2] Shuang Zhao,[1] Yu Zhou,[2,3,4] and Jun-Feng Wang[1,*]

[1]College of Physics, Sichuan University, Chengdu 610065, China
[2]Ministry of Industry and Information Technology Key Lab of Micro-Nano Optoelectronic Information System, Guangdong Provincial Key Laboratory of Semiconductor Optoelectronic Materials and Intelligent Photonic Systems, Harbin Institute of Technology, Shenzhen, 518055, China
[3]Quantum Science Center of Guangdong-Hong Kong-Macao Greater Bay Area (Guangdong), Shenzhen 518045, China
[4]zhouyu2022@hit.edu.cn
[†]These authors contributed equally to this Letter.
*jfwang@scu.edu.cn

Received 4 March 2024; revised 16 April 2024; accepted 29 April 2024; posted 29 April 2024; published 22 May 2024

Over the past decades, spin qubits in silicon carbide (SiC) have emerged as promising platforms for a wide range of quantum technologies. The fluorescence intensity holds significant importance in the performance of quantum photonics, quantum information process, and sensitivity of quantum sensing. In this work, a dual-layer Au/SiO_2 dielectric cavity is employed to enhance the fluorescence intensity of a shallow silicon vacancy ensemble in 4H-SiC. Experimental results demonstrate an effective fourfold augmentation in fluorescence counts at saturating laser power, corroborating our theoretical predictions. Based on this, we further investigate the influence of dielectric cavities on the contrast and linewidth of optically detected magnetic resonance (ODMR). There is a 1.6-fold improvement in magnetic field sensitivity. In spin echo experiments, coherence times remain constant regardless of the thickness of dielectric cavities. These experiments pave the way for broader applications of dielectric cavities in SiC-based quantum technologies.

https://doi.org/10.1364/OL.522770

Introduction. In recent years, color centers in SiC have attracted considerable attention in quantum technologies [1–11]. Particularly, the silicon vacancy in SiC has been widely used in various quantum technologies due to its exceptional properties such as near-infrared fluorescence and long coherence time [3,8,10]. The silicon vacancy is a spin qubit ($S = 3/2$) consisting of a missing silicon atom in 4H or 6H SiC lattices [3,7,8,10]. However, the missing silicon atom may be on hexagonal h-lattice points or quasi-cubic k-lattice points, which corresponds to two types of silicon vacancies, V1 and V2. The zero phonon lines of V1 and V2 are 861 nm and 915 nm, respectively. The zero-field splitting (ZFS) 2D of V1 and V2 is 4 MHz and 70 MHz, respectively [3,4,12]. Since the spin state of the V2 centers can be read out at room temperature and the ZFS remains constant as the temperature increases from 20 to 500 K [12,13], a significant portion of the prior research has concentrated on the V2 centers [3,7,8,10]. Therefore, we conduct our study using the V2 center throughout this work. In quantum photonics, the silicon vacancy in SiC has been coupled to various photonics structures, achieving the Purcell enhancement and nonlinear photonics [7,14]. In quantum information processing, the nuclear quantum register has been realized [8]. A high-fidelity spin–photon interface has successfully demonstrated its potential for constructing a scalable quantum network [15]. Furthermore, the utilization of silicon vacancies has been extended to a wide range of quantum sensing applications, such as magnetic field [16–18], temperature [13,19,20], and high-pressure magnetic detection [10]. Particularly, optically detected magnetic resonance (ODMR)-based nanotesla magnetometry has been achieved by utilizing a silicon vacancy ensemble generated through the thermal quenching method [18].

The fluorescence intensity is important for various quantum technologies. However, the maximum count achievable from a single silicon vacancy is only approximately 10 kcps, limiting its potential applications in quantum information [3]. Consequently, several approaches have been devised to augment the counts. Recently, the scalable-fabricated solid immersion lenses (SILs) have enhanced the counts by 2–4 times [3,21,22]. Scalable 800 nm high nanopillars with diameters ranging from 400 to 1400 nm enhance the counts by about three times [23]. Photonic crystal cavities have been employed to achieve an 80-fold Purcell enhancement of the ZPL of silicon vacancies [7,14,24]. However, all the methods require intricate micro-nanofabrication technologies, and achieving alignment between the silicon vacancy and the optimal mode position of photonic structures remains a challenging task [3,14,23–26]. The aforementioned points induce the non-ideal enhancement.

In this work, we achieve a significant increase in the counts of a shallow silicon vacancy ensemble in 4H-SiC by implementing a two-layer Au/SiO_2 dielectric cavity [27–29]. The counts exhibit variations depending on the thickness of SiO_2 films, with an optical fourfold enhancement observed at 20 nm at the saturating laser power. Based on this, we conduct a comparison of the ODMR between a bare SiC and a dielectric cavity, under

varying microwave power levels. Finally, we conduct measurements on spin echo signals of silicon vacancies, observing that the coherence time T_2 remains constant across different thicknesses of dielectric cavities. The above findings demonstrate that the dielectric cavity effectively increases the counts of silicon vacancies while maintaining the coherence time.

Experiments and results. In this study, we conduct experiments using a homemade room-temperature confocal scanning microscope equipped with a microwave system [10,13,30]. A laser with a wavelength of 785 nm is employed as the optical source. A 0.65 numerical aperture infrared objective is utilized to concentrate the laser beam that is reflected from the long-pass dichroic mirror (DM) onto the surface of the SiC sample, thereby inducing fluorescence in the silicon vacancy. The emitted fluorescence is directed through the DM and an 850 nm long-pass filter before being coupled to the single-photon counting module via a single-mode fiber for fluorescence counting. For the ODMR and spin echo experiments, the fluorescence is collected using a Femto instrument [10,13,30]. Standard lock-in techniques are employed for the detection of spin signals [10,13,30]. Silicon vacancy defects were created by introducing 30 keV carbon ions into high-purity 4H-SiC through ion implantation, with a dose of 1×10^{13} cm^{-2}. According to the results obtained from the stopping and range of ions in matter (SRIM) simulation, it can be inferred that the depth of the generated silicon vacancies is approximately 60 nm [31]. The SiC sample is subjected to annealing in a vacuum at 600°C for 2 h, enhancing the silicon vacancy density by approximately fourfold [30]. The estimated final density of the defects is approximately 3500 μm^{-2} and the conversion efficiency is about 3.5%. In recent years, the metal/SiO_2 dielectric cavity has emerged as a promising approach to enhance the fluorescence counts of the NV center in nanodiamonds [28] and two-dimensional materials [29]. This is achieved by manipulating the distribution of the electric field intensity at localized hot spots. Additionally, it can also manipulate the transfer of energy between nano-emitters and monolayer graphene [27]. The effective working range of the dielectric cavities can achieve 100 nm, making it suitable for manipulating deep color centers [28]. In this work, we employ a new type of dielectric cavity to amplify the fluorescence intensity of shallow silicon vacancies. The schematic of the device's structure is depicted in Fig. 1(a). Both SiO_2 and Au films are deposited using the RF magnetron sputter method [27–29]. In order to utilize a copper wire with a diameter of 50 μm transmitting microwave signals to manipulate the spin of silicon vacancies, we fabricate some gaps in Au/SiO_2 cavities.

The fluorescence intensity is related to the product of both excitation and emission bands of the electric field intensity [27–29,32]. To demonstrate the enhancement effect of the Au/SiO_2 cavity, we utilize the three-dimensional finite-difference time-domain (3D-FDTD) method to simulate the spatial distribution of electric field intensity for both the excitation (785 nm) and emission (940 nm) peaks of SiCs [28,29]. In the FDTD region, the grid size in the z-direction is set to 1 nm, whereas the grid size in the x- and y-directions is set to 40 nm. To predict the distribution of fluorescence emission intensity in SiC, we directly calculate the product of the distribution of both excitation and emission bands at each point. The average value of the fluorescence emission intensity at $z = 60$ nm represents the relative fluorescence intensity of silicon vacancies. The simulation of the bare SiC and the 20 nm SiO_2 sample is depicted in Figs. 1(b) and 1(c), respectively, demonstrating at least a fourfold enhancement in the electric field intensity.

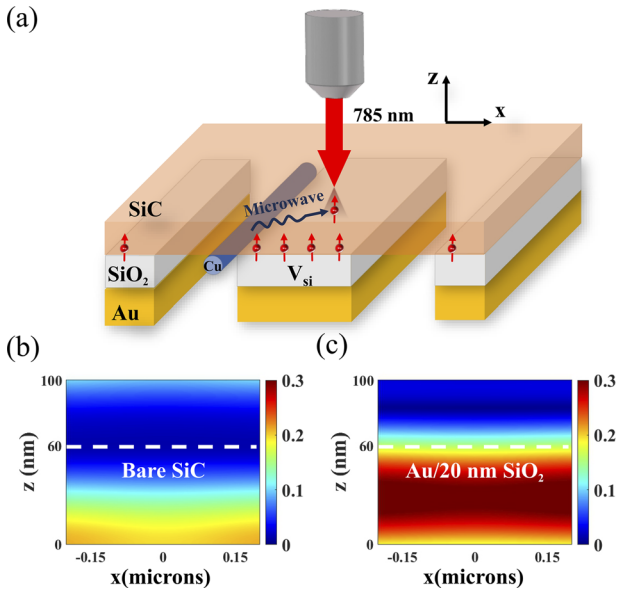

Fig. 1. Schematic of the sample. (a) Schematic of the sample device's structure. The objective lens is to focus the pump laser beam and collect the fluorescence. The direction of the silicon vacancy spin is parallel to the c axis. Different thicknesses of SiO_2 films are deposited on the sample surface. The 150 nm Au film is deposited on the SiO_2 film. A 50 μm diameter copper wire is fabricated on the sample surface to transmit microwave and manipulate spins of the silicon vacancy. (b) and (c) Electric field distribution of the bare SiC and the 20 nm SiO_2 sample, respectively. The dashed lines represent the depth of the silicon vacancy.

Then, the fluorescence counts of different samples are measured to analyze the enhancement effect. Since the optimal counts of the single silicon vacancy do not exhibit any further increase beyond a laser power of about 4 mW [3], we scan the fluorescence counts of both the bare SiC and X nm SiO_2 samples with a laser power of 4 mW. As shown in Fig. 2(a), the fluorescence counts of the 20 nm SiO_2 sample exhibit the highest value among all the samples, with a nearly fivefold increase compared to the bare SiC sample. After the thickness of SiO_2 increases to 60 nm, the enhanced effect of dielectric cavities gradually diminishes, suggesting the existence of an optimal thickness for the cavity.

To investigate the fluorescence-enhanced effect of the Au/SiO_2 cavity under varying laser powers, we measure the saturating count curves as a function of laser powers. As depicted in Fig. 2(b), the counts of the bare SiC, 20 nm, and 100 nm SiO_2 samples are represented by the black, blue, and red dots, respectively. The black, blue, and red lines represent the corresponding fitting curves obtained by utilizing the function $I = I_S/(1+P_S/P)$, where I_S denotes the saturating count and P_S denotes the saturating laser power. The saturating counts I_S and laser powers P_S of the bare SiC and 20 nm SiO_2 samples are simulated to be 1.6 ± 0.1 Mcps and 4.5 ± 0.1 Mcps, 23.3 ± 0.7 mW, and 9.4 ± 0.3 mW, respectively. Moreover, the corresponding saturating laser powers decrease due to the assistance of Au/SiO_2 cavities' enhancement [33]. Subsequently, we compare the fluorescence intensity at the saturating laser power (23 mW) of the bare SiC

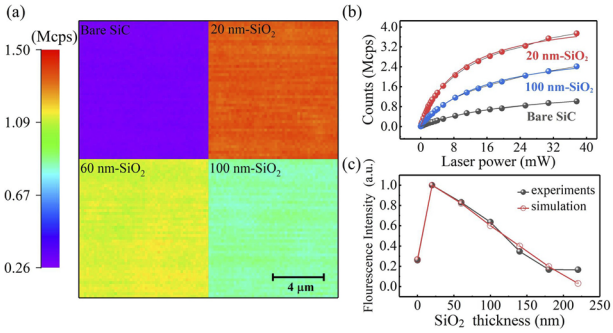

Fig. 2. Fluorescence counts of the samples. (a) Combinatorial confocal scanning microscopy image (10×10 μm^2) of spin defects of the bare SiC and Au/X nm SiO_2 sample (X = 20, 60, 100) at a 4 mW laser. (b) Saturating curves as a function of laser power of the bare SiC and 20 and 100 nm SiO_2 cavity samples. (c) Experimental and theoretical silicon vacancy fluorescence intensity of the bare SiC and different thicknesses (X = 20, 60, 100, 140, 180, 220 nm) of SiO_2 samples at 23 mW. The experimental counts are the mean values of scanning areas. The value of the ordinate is normalized by the fluorescence intensity of the 20 nm SiO_2 cavity sample, while the 0 nm SiO_2 represents the bare SiC sample.

and all SiO_2 samples with varying thicknesses theoretically and experimentally. As illustrated in the diagram in Fig. 2(c), the theoretical and experimental results exhibit a high degree of concurrence. Therefore, the dielectric cavity exhibits an optimal fourfold enhancement at SiO_2 20 nm [27,28].

The ODMR plays a crucial role in various quantum sensing applications [10,16–20,34]. To investigate the influence of Au/SiO_2 cavities on ODMR, we conduct measurements on both the 20 nm SiO_2 sample and the bare SiC. The ODMR spectra obtained at a microwave power of 22 dBm are shown in Fig. 3(a). The corresponding ZFSs are 72.6 and 72.7 MHz, respectively, which are in line with the previous work [3,12,32]. Moreover, the ODMR contrasts of the two samples are about 1.6×10^{-3} at 22 dBm, while the ODMR linewidth of the 20 nm SiO_2 sample (22.4 MHz) is a little wider than that of the bare SiC sample (17.5 MHz). The ODMR contrasts of the two samples at different microwave powers are summarized in Fig. 3(b), which exhibit prominent consistency. Both contrasts demonstrate an

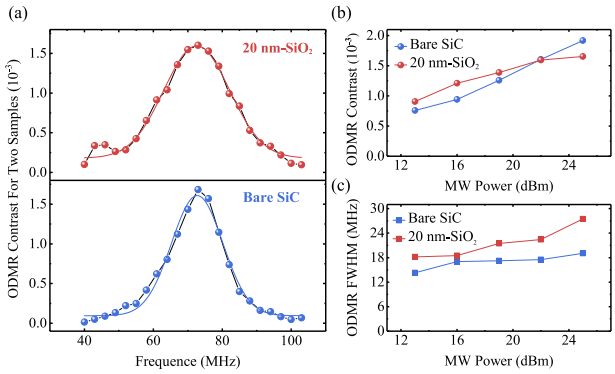

Fig. 3. Measurements of ODMR spectra for different samples. (a) ODMR spectra of silicon vacancy defects in the 20 nm SiO_2 sample and bare SiC without the external magnetic field at the microwave power of 22 dBm. (b) and (c) ODMR contrast and FWHM as a function of microwave power for the two samples, respectively.

increase as the microwave power is elevated. Hence, the integrated Au/SiO_2 cavity does not adversely impact the ODMR contrast [31,33]. Next, we investigate the cavities' impact on the ODMR linewidth. As depicted in Fig. 3(c), the linewidths of different samples exhibit an increase with the rise in the microwave power. Moreover, the FWHM of the 20 nm SiO_2 sample is slightly higher than the bare SiC. Additionally, the sensitivity of ODMR-based magnetic field sensing is determined by the following equation [18]:

$$\eta_B = \frac{4}{3\sqrt{3}} \frac{h}{g\mu_B} \frac{\Delta}{C\sqrt{R}}, \tag{1}$$

where g is the Landé factor for the V_{Si} spin defect; h and μ_B are Planck's constant and the Bohr magneton, respectively; R is the rate of detected photons; C is the ODMR contrast; and Δ is the ODMR linewidth. Combined with our experimental data, the magnetic sensitivity (at 4 mW) for 20 nm cavities and bare SiCs is 330 μT/Hz$^{1/2}$ and 610 μT/Hz$^{1/2}$, respectively, leading to a 1.8 times enhancement. At a saturating laser power of 23 mW, the enhancement factor is about 1.6. Nevertheless, the dielectric cavity holds great potential for enhancing the sensitivity of ODMR-based magnetic field and temperature sensing [18–20,35].

The stable spin coherent property of the silicon vacancy is essential in quantum information technologies [1–3,9,10]. To investigate the impact of Au/SiO_2 cavities, we conduct measurements on various samples using the Hahn echo sequence [3,10,13] under a static magnetic field of 40 G. The obtained results for the bare SiC and Au/60 nm SiO_2 cavity samples are presented in Figs. 4(a) and 4(b). Based on the fitting analysis, the T_2 values are determined to be 5.0 ± 0.7 μs and 5.3 ± 0.7 μs, respectively. To further indicate whether the different thicknesses of the cavity affect spin coherence time, the corresponding T_2 for all samples are depicted in Fig. 4(c). The T_2 remains invariable as a function of SiO_2 thicknesses, exhibiting slight fluctuations around the mean value of 5.2 μs. The findings demonstrate that the Au/SiO_2 cavity does not affect the spin coherence times of silicon vacancies, which is important for the advancement of SiC-based quantum technologies.

Conclusion. In summary, we investigate the optical and spin characteristics of a shallow silicon vacancy ensemble in 4H-SiC using a two-layer Au/SiO_2 dielectric cavity. Through manipulating the thickness of SiO_2, a significant fourfold increase in the counts at the SiO_2 20 nm is achieved. This is consistent with our theoretical simulations. Additionally, the Au/SiO_2 dielectric cavity can immediately be used to enhance the counts of the single silicon vacancy [3,23] and divacancy [1,2] and NV center [11,36] in SiCs. Although we use the bulk sample in the experiment, the SiC thin layer with spin qubits has been fabricated [33,37]. As a result, the simple cavity method can be easily applied to a thin layer sample. The ODMR experiments indicate that the contrast is almost identical for both the bare SiC and the optimal dielectric cavities. Moreover, the magnetic field sensitivity experiences about a 1.6-fold enhancement at the saturating laser power. Finally, the spin echo experiments demonstrate that the coherence time is unaltered despite variations in the SiO_2 thickness. Our finding suggests that a straightforward dielectric cavity can effectively enhance the emission of spin qubits in SiC while maintaining spin properties intact. The experiments give the basis for the utilization of dielectric cavities in SiC-based quantum information.

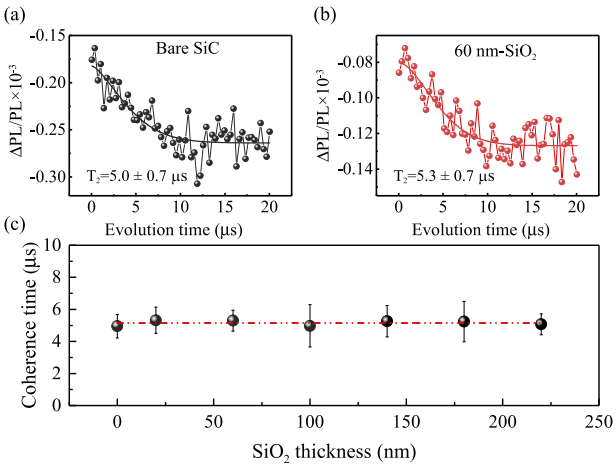

Fig. 4. Spin coherence time measurements for all samples. (a) and (b) Hahn echo measurements of the bare SiC and 60 nm SiO_2 samples at a magnetic field of 40 G. The lines are the exponential decay fits to the data. (c) Spin coherence times as a function of the SiO_2 cavity thickness.

Funding. National Natural Science Foundation of China (11975221, 12304568, 61905233); Basic and Applied Basic Research Foundation of Guangdong Province (2022A1515110382); Science Specialty Program of Sichuan University (2020SCUNL210); Shenzhen Fundamental Research Program (No. JCYJ20230807094408018); Guangdong Provincial Quantum Science Strategic Initiative (GDZX2303001, GDZX2200001).

Disclosures. The authors declare no conflicts of interest.

Data availability. Data underlying the results presented in this paper are not publicly available at this time but may be obtained from the authors upon reasonable request.

Supplemental document. See Supplement 1 for supporting content.

REFERENCES

1. W. F. Koehl, B. B. Buckley, F. J. Heremans, *et al.*, Nature **479**, 84 (2011).
2. D. J. Christle, A. L. Falk, P. Andrich, *et al.*, Nat. Mater. **14**, 160 (2015).
3. M. Widmann, S.-Y. Lee, T. Rendler, *et al.*, Nat. Mater. **14**, 164 (2015).
4. E. Janzén, A. Gali, P. Carlsson, *et al.*, Phys. B **404**, 4354 (2009).
5. A. Lohrmann, B. Johnson, J. McCallum, *et al.*, Rep. Prog. Phys. **80**, 034502 (2017).
6. J. Wang, Y. Zhou, Z. Wang, *et al.*, Nat. Commun. **9**, 4106 (2018).
7. D. M. Lukin, C. Dory, M. A. Guidry, *et al.*, Nat. Photonics **14**, 330 (2020).
8. C. Babin, R. Stöhr, N. Morioka, *et al.*, Nat. Mater. **21**, 67 (2022).
9. A. Bourassa, C. P. Anderson, K. C. Miao, *et al.*, Nat. Mater. **19**, 1319 (2020).
10. J.-F. Wang, L. Liu, X.-D. Liu, *et al.*, Nat. Mater. **22**, 489 (2023).
11. J.-F. Wang, F.-F. Yan, Q. Li, *et al.*, Phys. Rev. Lett. **124**, 223601 (2020).
12. R. Nagy, M. Widmann, M. Niethammer, *et al.*, Phys. Rev. Appl. **9**, 034022 (2018).
13. J.-F. Wang, F.-F. Yan, Q. Li, *et al.*, Nat. Commun. **12**, 3223 (2021).
14. D. O. Bracher, X. Zhang, and E. L. Hu, Proc. Natl. Acad. Sci. U. S. A. **114**, 4060 (2017).
15. R. Nagy, M. Niethammer, M. Widmann, *et al.*, Nat. Commun. **10**, 1 (2019).
16. M. Niethammer, M. Widmann, S.-Y. Lee, *et al.*, Phys. Rev. Appl. **6**, 034001 (2016).
17. D. Simin, V. Soltamov, A. Poshakinskiy, *et al.*, Phys. Rev. X **6**, 031014 (2016).
18. J. B. Abraham, C. Gutgsell, D. Todorovski, *et al.*, Phys. Rev. Appl. **15**, 064022 (2021).
19. A. Anisimov, D. Simin, V. Soltamov, *et al.*, Sci. Rep. **6**, 33301 (2016).
20. T. M. Hoang, H. Ishiwata, Y. Masuyama, *et al.*, Appl. Phys. Lett. **118**, 044001 (2021).
21. F. Sardi, T. Kornher, M. Widmann, *et al.*, Appl. Phys. Lett. **117**, 022105 (2020).
22. C. Bekker, M. J. Arshad, P. Cilibrizzi, *et al.*, Appl. Phys. Lett. **122**, 173507 (2023).
23. M. Radulaski, M. Widmann, M. Niethammer, *et al.*, Nano Lett. **17**, 1782 (2017).
24. A. L. Crook, C. P. Anderson, K. C. Miao, *et al.*, Nano Lett. **20**, 3427 (2020).
25. G. Calusine, A. Politi, and D. D. Awschalom, Phys. Rev. Appl. **6**, 014019 (2016).
26. M. N. Gadalla, A. S. Greenspon, R. K. Defo, *et al.*, Proc. Natl. Acad. Sci. U. S. A. **118**, e2021768118 (2021).
27. J.-F. Wang, H.-L. Zhou, X. Xiong, *et al.*, Carbon **161**, 794 (2020).
28. S.-J. Kuo, P.-C. Tsai, Y.-C. Lee, *et al.*, Nanoscale **10**, 17576 (2018).
29. Y.-C. Lee, Y.-C. Tseng, and H.-L. Chen, ACS Photonics **4**, 93 (2017).
30. J.-F. Wang, Q. Li, F.-F. Yan, *et al.*, ACS Photonics **6**, 1736 (2019).
31. Q. Li, J.-F. Wang, F.-F. Yan, *et al.*, Nanoscale **11**, 20554 (2019).
32. E. C. Le Ru and P. G. Etchegoin, Chem. Phys. Lett. **423**, 63 (2006).
33. J.-Y. Zhou, Q. Li, Z.-H. Hao, *et al.*, Nano Lett. **23**, 4334 (2023).
34. L. Liu, J.-F. Wang, X.-D. Liu, *et al.*, Nano Lett. **22**, 9943 (2022).
35. J.-F. Wang, J.-M. Cui, F.-F. Yan, *et al.*, Phys. Rev. B **101**, 064102 (2020).
36. H. Von Bardeleben, J. Cantin, E. Rauls, *et al.*, Phys. Rev. B **92**, 064104 (2015).
37. W.-K. Quan, L. Liu, Q.-Y. Luo, *et al.*, Opt. Lett. **48**, 1423 (2023).